



ELSEVIER

Available online at www.sciencedirect.com

SCIENCE @ DIRECT®

Journal of Computational Physics 194 (2004) 481–504

JOURNAL OF
COMPUTATIONAL
PHYSICS

www.elsevier.com/locate/jcp

Perfectly matched layers for radio wave propagation in inhomogeneous magnetized plasmas

Natalia A. Gondarenko ^{a,*,1}, Parvez N. Guzdar ^a, Sidney L. Ossakow ^b,
Paul A. Bernhardt ^b

^a *Institute for Research in Electronics and Applied Physics, University of Maryland, College Park, MD 20742-3511, USA*

^b *Plasma Physics Division, Naval Research Laboratory, Washington, DC 20375-5346, USA*

Received 8 January 2003; received in revised form 1 September 2003; accepted 5 September 2003

Abstract

We present 1D and 2D numerical models of the propagation of high-frequency (HF) radio waves in inhomogeneous magnetized plasmas. The simulations allow one to describe the process of linear conversion of HF electromagnetic waves into electrostatic waves. The waves, launched from the lower boundary normally or at a specified angle on a layer of a magnetoactive plasma, can undergo linear conversion of the incident *O*-mode into a *Z*-mode at appropriate locations in an inhomogeneous prescribed plasma density. The numerical scheme for solving 2D HF wave propagation equations is described. The model employed the Maxwellian perfectly matched layers (PML) technique for approximating nonreflecting boundary conditions. Our numerical studies demonstrate the effectiveness of the PML technique for transparent boundary conditions for an open-domain problem.

© 2003 Elsevier Inc. All rights reserved.

1. Introduction

The modelling of radio wave propagation in inhomogeneous ionospheric plasmas is of the great importance in a number of ionospheric experiments relevant to communication, radar and navigation systems. Many practical problems of the interaction of HF radio waves in the ionosphere involve the study of the structure and the amplitude of the fields near reflection or resonance regions. The density irregularities can significantly affect radio wave propagation [1]. At the lower altitudes of the ionosphere, the *E* region, the 2D images of sporadic-*E* layers have been produced with radio-induced fluorescence (RIF) technique [2,3]. Bernhardt has developed a theory to explain the generation of the structures in the RIF images interpreted as modulation in the ion-layer densities [4]. In our numerical experiments, we use the 2D electron

* Corresponding author. Tel.: +1-301-405-1621.

E-mail address: ngondare@umd.edu (N.A. Gondarenko).

¹ This research was supported by the Office of Naval Research.

density profile, which is an approximation of the electron density of sporadic-*E* layer obtained from numerical computations of the modulation of the ion-layers by the Kelvin–Helmholtz instability in the neutral atmosphere [4].

In ionospheric modification experiments, the evolution of the electron density affects the propagation of HF radio waves and therefore it is necessary to find solutions of the electromagnetic fields varying slowly on the time scale of the density evolution. These ionospheric modification experiments investigated nonlinear effects in the ionosphere, as an example, the excitation of irregularities in the ionosphere by radio wave heating, which has been attributed to the thermal self-focusing instability (SFI). The first 2D model of the thermal SFI by Bernhardt and Duncan [5] was for underdense plasmas, where the instability is convective in character. Guzdar et al. [6] and Gondarenko et al. [7] simulated the propagation of HF radio waves in an inhomogeneous gyrotropic medium near the reflection height, where the thermal SFI is an absolute instability. They used a simplified model by assuming that the wave was incident normally and propagated vertically along the magnetic field and the direction of inhomogeneity.

Numerical modelling of the propagation of radio waves in anisotropic inhomogeneous ionospheric plasmas requires solving the time-dependent Maxwell's equations in a computational domain with perfectly conducting boundaries. In many radio wave propagation investigations, only one boundary of the calculation domain (usually the lower one) is a physical boundary, and the upper boundary must be perfectly transparent. For the 2D case, the side boundaries can also be transparent allowing for the waves to propagate out of the computational domain through them. It is a known fact that such nonreflecting boundaries can cause significant numerical challenges in computations and, if not implemented correctly, can lead to spurious results.

In the earliest implementations of nonreflecting boundaries, the standard approach was to use absorbing layers above the physical computational region. In these layers, the numerical solution is damped by the application of filters or other numerical damping techniques [8,9]. Even though with this method of energy absorption in real space one can achieve satisfactory results in reducing the reflection coefficients, for many wave propagation problems this method becomes very expensive in computational cost since it requires a significant increase in the size of the calculation domain.

Another type of widely accepted method for a nonreflecting boundary is based on perfectly matched layers (PMLs), and was first introduced by Berenger [10]. The new matched medium (called perfectly matched) was designed so that the theoretical reflection factor of a plane wave propagating through the interface between the physical domain and the new computational layer is zero at any frequency and at any angle of incidence. This method requires a small number of grid points in order to achieve satisfactory results. The energy of the outgoing wave is absorbed within the PML region where the fields exponentially decay, and this can reduce the reflection coefficient for any angle of incidence [11]. The reflectionless properties of PML are discussed in detail by Chew and Weedon [12]. They showed that the PML could be related to a complex stretching of the Cartesian coordinates in the frequency domain. This method of implementation of nonreflecting boundary conditions is referred to as the Maxwellian PML. In the Berenger implementation of the PML technique for the numerical solution of the unbounded electromagnetic problems with a finite-difference time-domain method, the electromagnetic fields in the equations were split into subcomponents. Thus with the introduction of additional equations for the subcomponents of the fields, which do not satisfy Maxwell's equations, a new set of equations have to be solved. This is the so-called non-Maxwellian version of PML. An unsplit-field implementation of PML requires solving the Maxwell's equations derived by modifying the medium with complex anisotropic permittivity tensor [13,14], so that the new normalized fields obey the Maxwell's equations. In this paper, we use the Maxwellian formulation of PML.

The numerical scheme applied for our simulations is based on the implicit Crank–Nicholson finite-difference (FD) scheme. The implementation of this type of scheme permits the modelling of arbitrary boundary conditions. In the 1D case, we use the so-called Thomas algorithm for solving tridiagonal system

of linear equations, which arise from the implicit finite-difference approximation of the 1D scalar equations. The stability of this type of algorithms and their modifications are described by Godunov and Ryabenkii [15], Isaacson and Keller [16], Richtmyer and Morton [17]. For the solution of FD 1D vector equations we use algorithms discussed by Isaacson and Keller [16] and Samarskii [18]. Finite-difference equations for a vector model in two dimensions are solved with the alternating direction implicit (ADI) method. The ADI methods for solving the parabolic and elliptic partial differential equations (PDEs) in 2D space were first developed by Peaceman and Rachford [19], Douglas and Rachford [20]. Later, McKee and Mitchell [21] included a mixed cross-derivative term in the 2D parabolic PDEs.

In Section 1 of this paper, we discuss the computational models arising in the simulations of radio wave propagation in the ionospheric plasmas. In Section 2, for the general case when a wave is incident obliquely on a plane layer of cold magnetoactive plasma, the system of equations and the dispersion equation representing the four modes of the wave propagation are presented. The implementation of the Maxwellian formulation of the PML technique is discussed in Section 3. In Section 4, we introduce the boundary conditions that account for the amplitude and the phase of the upward going wave. In the following Sections 5 and 6, the algorithms for the scalar and vector equations for the wave propagation in inhomogeneous isotropic and magnetized plasmas are described. In Section 7, the composite scheme for solving 2D vector equations with complex coefficients is derived. Finally, in Sections 8 and 9, we present the numerical examples of radio wave propagation for 1D and 2D inhomogeneous density profiles, demonstrating the effectiveness of the PML technique. Section 10 has the concluding remarks.

2. Basic wave propagation equations

Let us consider the problem of the HF radio wave propagation in the ionosphere. To describe electromagnetic fields we shall use the averaged values of the electric and magnetic fields. In wave propagation in the ionosphere, the plasma field wavelengths are large compared with the mean distance between particles so that the statistical averaging is equivalent to averaging over a sufficiently small volume. For monochromatic fields $\vec{E}(r, t) = \vec{E}(r)e^{-i\omega t}$, the statistically averaged field equations (Maxwell's curl equations) are the following:

$$\nabla \times \vec{H} = \frac{4\pi}{c} \vec{j} - i \frac{\omega}{c} \vec{D}, \tag{1}$$

$$\nabla \times \vec{E} = i \frac{\omega}{c} \vec{H}, \tag{2}$$

where \vec{E} is the electric field, \vec{H} is the magnetic field, \vec{D} is the electric field displacement, and \vec{j} is the induced current density. \vec{D} and \vec{j} related to \vec{E} through the hermitian tensors ϵ_{ij} and σ_{ij} :

$$D_i = \epsilon_{ij} E_j, \quad j_i = \sigma_{ij} E_j.$$

Here spatial dispersion is neglected, so that relation between \vec{D} and \vec{j} and \vec{E} is local. Finally, taking the curl of Eq. (1) and using Eq. (2), we derived the wave equations for the electromagnetic waves for a “cold” plasma medium [23]:

$$-\nabla^2 \vec{E} + \vec{\nabla}(\nabla \cdot \vec{E}) = \frac{\omega^2}{c^2} \left(\vec{D} + i \frac{4\pi}{\omega} \vec{j} \right), \tag{3}$$

$$D_i + i \frac{4\pi}{\omega} j_i = \epsilon'_{ij} E_j,$$

where $\varepsilon'_{ij}(\omega) = \varepsilon_{ij}(\omega) + i\frac{4\pi}{\omega}\sigma_{ij}(\omega)$ is the complex permittivity tensor describing electromagnetic properties of a plasma in a magnetic field, σ_{ij} is the conductivity tensor. In the coordinate system we have used, the z -axis is along the density gradient, and the magnetic field $H^{(0)}$ is in the xz -plane (the plane of magnetic meridian). The magnetic field makes an angle α with the z -axis, and in the case of normal incidence, the HF radio wave is launched vertically upward (parallel to the z -axis).

Let us consider propagation of a plane wave $\vec{E} = \vec{E}_0 e^{i(-\omega t + \vec{k}\cdot\vec{r})}$, where \vec{k} is the wave vector. For homogeneous plane waves, the planes of equal phase and amplitude coincide, and $k = \frac{\omega}{c}(n - i\mu)$, where n and μ are the indices of refraction and absorption, respectively. Then, Eq. (3) becomes

$$\left(\vec{D} + i\frac{4\pi}{\omega}\vec{j}\right) = (n - i\mu)^2(\vec{E} - \vec{s}(\vec{s}\cdot\vec{E})) \equiv (n - i\mu)^2(\vec{E} - \vec{k}(\vec{k}\cdot\vec{E})/k^2),$$

where $\vec{s} = \vec{k}/k$ is a real unit vector. This matrix equation can be solved to determine the dispersion relation for modes in a homogeneous magnetized plasma. In the case of a 1D inhomogeneous plasma (when permittivity depends only on height, the z -coordinate) for oblique incidence, when a wave is launched at a finite angle θ_0 , we can use the Eikonal representation $\vec{E} = \vec{E}_0 e^{-i\omega t + i\omega(p_0 x + \psi(z))/c}$ for the wave. The “local” wave vector in the plane of the magnetic meridian is $\vec{k} = \frac{\omega}{c}(p_0, 0, q)$, where $p_0 = \frac{\omega}{c}k_x = \sin\theta_0$, and $q = (d\psi/dz)$. Thus for this case,

$$(d\psi/dz)^2 + p_0^2 = (n - i\mu)^2,$$

which leads to a quartic equation for $q = d\psi/dz$ [23]:

$$\alpha q^4 + \beta q^3 + \gamma q^2 + \delta q + d = 0. \quad (4)$$

The solution of this dispersion equation represents the four modes of the wave propagation, namely, the upward and the downward propagating ordinary O -mode and the extraordinary X -mode. An O -mode, launched from the lower boundary, can be reflected at a plasma cutoff with the wave frequency equal to the plasma frequency at a certain height. For oblique propagation, the O -mode can be converted into the second branch of the extraordinary (X) mode, which in the ionospheric context is referred to as the Z -mode [24,25]. The extraordinary Z -mode is reflected at another cutoff and then it propagates to a plasma resonance region where it is converted into an electrostatic mode.

Finally, for the general case of a 2D problem (the permittivity is a function of both x and z coordinates), the basic equations for the electromagnetic wave propagating in a cold magnetoactive plasma are [23]:

$$-\frac{\partial^2 E_x}{\partial z^2} + \left(\frac{\partial}{\partial x} + ik_{x_0}\right)\frac{\partial E_z}{\partial z} - \frac{\omega^2}{c^2}(\varepsilon_{xx}E_x + \varepsilon_{xy}E_y + \varepsilon_{xz}E_z) = 0, \quad (5)$$

$$-\frac{\partial^2 E_y}{\partial z^2} + \left(\frac{\partial}{\partial x} + ik_{x_0}\right)^2 E_y - \frac{\omega^2}{c^2}(\varepsilon_{yx}E_x + \varepsilon_{yy}E_y + \varepsilon_{yz}E_z) = 0, \quad (6)$$

$$\left(\frac{\partial}{\partial x} + ik_{x_0}\right)^2 E_z + \left(\frac{\partial}{\partial x} + ik_{x_0}\right)\frac{\partial E_x}{\partial z} - \frac{\omega^2}{c^2}(\varepsilon_{zx}E_x + \varepsilon_{zy}E_y + \varepsilon_{zz}E_z) = 0, \quad (7)$$

where $k_{x_0} = \omega p_0/c$ is the x component of the wave vector at the lower boundary on which the incident wave is specified. Thus again the quartic equation (4) can be used at the lower boundary to determine the values of q relevant to the appropriate mode (O or X) of propagation.

In the next two sections we will discuss the discrete representations and the numerical algorithms to solve Eqs. (5)–(7) with nonreflecting PML boundary conditions for the 1D and 2D cases.

3. Perfectly matched layer implementation

In order to provide the nonreflecting boundary condition for an open-domain problem, a thin “absorbing” layer called the PML layer is added to the calculation domain above the height z_{pml} (in z -direction), separating the given medium and an artificial absorbing medium. In the following development, Eqs. (5)–(7) for the wave propagation are solved in the computation domain including the PML layer. In contrast to Berenger’s implementation of PML [10], the field components are unsplit in the entire calculation area.

Our implementation of the PML technique is similar to the one that has been used more recently for many computational problems [12–14]. Thus following this technique, Eqs. (5)–(7) are modified with a new set of complex stretching variables. The final solutions for the field components of Eqs. (5)–(7) are unchanged in the non-PML region of the computational domain and the solutions are evanescent in the thin PML layer. The new complex coordinates are defined as

$$\tilde{\xi} = \xi + i \int_0^\xi \gamma(\xi') d\xi',$$

where ξ is in the vertical z -direction (for our specific case), $\gamma(\xi) > 0$ within the PML medium above the height z_{pml} , and it is zero in the non-PML regions of the computation domain. The large imaginary component of the $\gamma(\xi)$ profile provides a fast absorption of the energy in the PML region with respect to the length of the absorbing layer. The function $\gamma(\xi)$ plays a role of a damping factor and it depends on the frequency ω , $\gamma = \sigma^E/\omega\epsilon_0 = \sigma^M/\omega\mu_0$, where σ^E and σ^M are the electric and the magnetic conductivities satisfying the matching impedance condition [10].

In the general case with a new set of complex coordinates, the operator nabla in Eq. (3) is the following:

$$\tilde{\nabla} = \hat{x} \frac{\partial}{\partial \tilde{x}} + \hat{y} \frac{\partial}{\partial \tilde{y}} + \hat{z} \frac{\partial}{\partial \tilde{z}},$$

where for the 2D example,

$$\frac{\partial}{\partial \tilde{z}} = \frac{1}{1 + i\gamma_z(z)} \frac{\partial}{\partial z}, \quad \frac{\partial}{\partial \tilde{x}} = \frac{1}{1 + i\gamma_x(x)} \frac{\partial}{\partial x}.$$

To formalize the transformation of the equation with the stretched coordinate we introduce the diagonal tensor \tilde{S} and the transformed complex permittivity tensor $\tilde{\epsilon}_{\text{pml}}$ [26,27]

$$\tilde{S} = \begin{bmatrix} \frac{1}{s_x} & 0 & 0 \\ 0 & \frac{1}{s_y} & 0 \\ 0 & 0 & \frac{1}{s_z} \end{bmatrix}, \quad \tilde{\epsilon}_{\text{pml}} = \det(\tilde{S})^{-1} (\tilde{S} \cdot \epsilon \cdot \tilde{S}) = \begin{bmatrix} \frac{s_y s_z}{s_x} \epsilon_{xx} & S_z \epsilon_{xy} & S_y \epsilon_{xz} \\ S_z \epsilon_{yx} & \frac{s_x s_z}{s_y} \epsilon_{yy} & S_x \epsilon_{yz} \\ S_y \epsilon_{zx} & S_x \epsilon_{zy} & \frac{s_x s_y}{s_z} \epsilon_{zz} \end{bmatrix},$$

where the complex stretching variables $s_x = 1 + i\gamma_x(x)$, $s_z = 1 + i\gamma_z(z)$, and $s_y = 1$ for our 2D case. The electric field components also should be transformed because in the complex space they are not Maxwellian, so that $\vec{E} \rightarrow \tilde{S}^{-1} \cdot \vec{E}$. Now \vec{E} is the electric field vector in the real space domain and satisfies the Maxwell equations with the transformed permittivity tensor $\tilde{\epsilon}_{\text{pml}}$. As would be expected, the new fields \vec{E} represent the absorbing behavior inside the PML layer and coincide with the original field solution of Eqs. (5)–(7) in the non-PML calculation domain.

4. Boundary conditions

In our calculation, the intensity of the incident radiation is given at the lower boundary for the 2D case or at the left boundary in the 1D case.

For the case of 1D wave propagation in an unmagnetized inhomogeneous plasma when a wave is incident normally, the plane wave solution of Eqs. (5)–(7) can be considered in the form $E_0 e^{ikz - i\omega t}$ with the amplitude E_0 . The solution of Eqs. (5)–(7) gives the dispersion relation and from this dispersion relation one can obtain the wave number k at the lower boundary

$$k = \pm \frac{1}{c} \left(\omega^2 - \omega_{\text{pe}}^2(z=0) \right)^{1/2}, \quad (8)$$

where ω_{pe} is the plasma frequency.

Let us consider the incident intensity at the left boundary, $z = 0$, as a sum of E_+ and E_- , the amplitudes of the upward and the downward propagating waves, respectively:

$$E = \hat{E}_+ e^{ikz} + \hat{E}_- e^{-ikz}. \quad (9)$$

Since the amplitude of the downward propagating wave is unknown, the elimination of E_- from both (9), and its differentiation over z , yields the expression for the boundary condition at $z = 0$, namely

$$\left. \frac{\partial E}{\partial z} \right|_{z=0} + ikE \Big|_{z=0} = 2ik\hat{E}_+, \quad (10)$$

where k is the wave number for the incident upward propagating wave. For this specific case, k is given by Eq. (8). In the anisotropic case, the amplitude of the electromagnetic wave is determined by the ordinary and extraordinary modes. For the general case, when the wave is incident obliquely on the layer, the expression for the wave number k is more complicated, and since Eq. (4) for the dispersion relation is fourth-order, there are four wave numbers for the four modes.

The boundary condition given by Eq. (10) is the mixed Dirichlet–Neumann boundary condition, and it can be easily implemented into a finite-difference approximation algorithm determining the recursion relations at $z = 0$ for the tridiagonal solver.

At the right boundary $z = L_z$, $E = 0$. However, because the PML layer is implemented at the right boundary to absorb the wave, there is no reflection from this boundary.

5. One-dimensional scalar equations for wave propagation in inhomogeneous isotropic plasmas

To illustrate how the PML technique may be used in the finite-difference implementation of wave propagation equations, let us consider the 1D wave propagation in an isotropic plasma. This type of an equation can occur in acoustics or in the theory of wave propagation of any type. In the particular case of a wave incident normally on a layer of an inhomogeneous medium, the system of Eqs. (5)–(7) is reduced to one parabolic equation for either E_x or E_y . In this case, the permittivity tensor $\epsilon'(\omega, z)$ has only diagonal elements, as does the transformed permittivity tensor $\tilde{\epsilon}_{\text{pml}}$. Therefore, the equation for E_x in the general form is the following:

$$\frac{\partial^2 E_x}{\partial z^2} + \frac{\omega^2}{c^2} \left(1 - \frac{\omega_{\text{pe}}^2}{\omega^2} N(z) \right) E_x = 0, \quad (11)$$

where $N(z)$ is the given density profile. In the general case, the electron density can vary with time, and therefore we shall find the solutions for the electromagnetic fields varying slowly on the time scale of the density evolution. We present the electric field as $E_x = E_{\infty x} e^{-i\omega_0 t}$. Since we consider the “slow” wave equations, the very fast time scales associated with the electromagnetic pump wave frequency ω are removed, and with this approximation one can write for the amplitude of the electromagnetic field

$$\frac{\partial^2 E_x}{\partial t^2} = -2i\omega_0 \frac{\partial E_{\infty x}}{\partial t} - \omega_0^2 E_{\infty x}.$$

Thus by substituting $\omega^2 = 2i\omega_0 \frac{\partial}{\partial t} + \omega_0^2$ into Eq. (11), the “slow” PML wave equation is written in the form of the time-dependent linear Schrödinger equation

$$\left[\frac{\partial}{\partial t} - i \frac{c^2}{2\omega_0} \frac{1}{s_z} \frac{\partial}{\partial z} \left(\frac{1}{s_z} \frac{\partial}{\partial z} \right) - i \frac{\omega_0}{2} \left(1 - \frac{\omega_{pe}^2}{\omega_0^2} N(z) \right) \right] E_{\infty x} = 0. \tag{12}$$

Finally, with normalizations of the spatial variable z to the Airy length, $z_0 = (c^2 L / \omega_0^2)^{1/3}$, and time t to $t_0 = 2\omega_0 z_0^2 / c^2$, where L is the scale length of the density inhomogeneity, the dimensionless 1D PML equation for wave propagation in an isotropic plasma is

$$\left[\frac{\partial}{\partial t} - i \frac{1}{s_z} \frac{\partial}{\partial z} \left(\frac{1}{s_z} \frac{\partial}{\partial z} \right) - i \frac{L}{z_0} \left(1 - \frac{\omega_{pe}^2}{\omega_0^2} N(z) \right) \right] E_{\infty x} = 0. \tag{13}$$

Eq. (13) is the model scalar Schrödinger type PDE that can be approximated with the Crank–Nicholson implicit finite-difference scheme. The application of this scheme results in the matrix equation

$$[T]\{E\} = \{D\},$$

where D contains the terms at the previous time step,

$$[T] = \text{tridiagonal}\{a_i, b_i, c_i\}$$

is the matrix of coefficients which depend on the particular finite difference approximation. For this specific case with the use of the Crank–Nicholson finite-difference approximation and with complex stretched variables, coefficients are defined as:

$$\begin{aligned} a_i &= -\bar{f}_i (\bar{f}_{i-1} + \bar{f}_i) \rho, \\ c_i &= -\bar{f}_i (\bar{f}_{i+1} + \bar{f}_i) \rho, \\ b_i &= \bar{f}_i (\bar{f}_{i-1} + 2\bar{f}_i + \bar{f}_{i+1}) \rho - 4i - 2 \frac{L \Delta_t}{z_0} \left(1 - \frac{\omega_{pe}^2}{\omega_0^2} N(z) \right), \end{aligned} \tag{14}$$

with $\rho = \Delta_t / \Delta_z^2$, Δ_t the time step, Δ_z the grid spacing, and the absorbing complex function

$$\bar{f}_i = \frac{1}{s_z} = \frac{1}{1 + i\gamma_z(z)}.$$

The von Neumann condition for stability of the FD scheme is $|\tilde{g}| \leq 1$, where \tilde{g} is an amplification factor. For the Crank–Nicholson FD approximation of the scalar Eq. (13) with $\gamma_z(z) = 0$, the amplification factor is complex, and we must take into account the magnitude of the amplification factor in the complex plane,

$$|\tilde{g}| = |(1 + i(1/2)\mathbf{H}) / (1 - i(1/2)\mathbf{H})| = 1.$$

Here \mathbf{H} is operator defined as $(\mathbf{H}E)_i \equiv \rho(\delta^2 E)_i + \Delta_t V_i E_i$, V_i is variable coefficient. It follows that von Neumann condition is always satisfied, so that the Crank–Nicholson method is unconditionally stable.

In the PML layer $\gamma_z(z) \neq 0$. Assuming it to be a constant, the operator \mathbf{H} is defined as $(\mathbf{H}E)_i \equiv \rho((1 - \gamma^2)/(1 + \gamma^2)^2)(\delta^2 E)_i - i\rho(2\gamma/(1 + \gamma^2)^2)(\delta^2 E)_i + \Delta_t V_i E_i$. In this case, with $\delta^2 E = -4 \sin^2(\phi/2)E$ (where $\phi = m_z \Delta_z$, m_z is the wave number), simple algebra gives

$$|\tilde{g}|^2 = 1 - 16\gamma\rho \sin^2(\phi/2)/((1 + \gamma^2)^2 + 8\gamma\rho \sin^2(\phi/2) + 4\rho^2 \sin^4(\phi/2)).$$

One can see that $|\tilde{g}| < 1$ for $\gamma > 0$ and thereby justify that the Crank–Nicholson scheme is stable.

To solve the tridiagonal system of linear equations arising from FD approximation, we use an efficient algorithm that is referred to as the Thomas algorithm mentioned above [15–17].

6. One-dimensional vector equations for wave propagation in inhomogeneous magnetoactive plasmas

In the general case, when the wave is incident obliquely on the layer of a magnetized plasma, Eq. (3) is the system of three second-order equations. Note that the electromagnetic fields vary slowly on the time scale of the density evolution. Thus, the normalized system of the slow wave equations in 2D is the following:

$$\frac{\partial E_x}{\partial t} = \left(i \frac{\partial^2}{\partial z^2} + i \frac{L}{z_0} \varepsilon_{xx} \right) E_x + \left(i \frac{L}{z_0} \varepsilon_{xy} \right) E_y + \left(k_{x_0} \frac{\partial}{\partial z} - i \frac{\partial^2}{\partial x \partial z} + i \frac{L}{z_0} \varepsilon_{xz} \right) E_z, \quad (15)$$

$$\frac{\partial E_y}{\partial t} = \left(i \frac{L}{z_0} \varepsilon_{yx} \right) E_x + \left(i \frac{\partial^2}{\partial x^2} + i \frac{\partial^2}{\partial z^2} - i k_{x_0}^2 + i \frac{L}{z_0} \varepsilon_{yy} \right) E_y + \left(i \frac{L}{z_0} \varepsilon_{yz} \right) E_z, \quad (16)$$

$$\frac{\partial E_z}{\partial t} = \left(k_{x_0} \frac{\partial}{\partial z} - i \frac{\partial^2}{\partial x \partial z} + i \frac{L}{z_0} \varepsilon_{zx} \right) E_x + \left(i \frac{L}{z_0} \varepsilon_{zy} \right) E_y + \left(i \frac{\partial^2}{\partial x^2} - i k_{x_0}^2 + i \frac{L}{z_0} \varepsilon_{zz} \right) E_z. \quad (17)$$

Here, $k_{x_0} = \sqrt{L/z_0} p_0$ is a constant and the external magnetic field H^0 is at an angle α to the z -axis. For normal incidence of the wave on the layer, $k_{x_0} = 0$, and the system of Eqs. (15)–(17) is simplified, becoming two second-order equations. Besides, for longitudinal or transverse propagation when $\alpha = 0^\circ$ or $\alpha = 90^\circ$, two second-order equations separate into two independent second-order equations, and so in these particular cases, they can be solved similar to the isotropic case.

In the case of normal incidence ($k_{x_0} = 0$) for the 1D wave propagation in the z -direction, the Schrödinger type equations (15)–(17) are solved with the methods described in [16–18]. The finite-difference approximation is applied to each Eqs. (15)–(17), resulting in a block-tridiagonal matrix equation

$$\tilde{A}_j \mathbf{Y}_{j-1} + \tilde{C}_j \mathbf{Y}_j + \tilde{B}_j \mathbf{Y}_{j+1} = \mathbf{F}_j, \quad j = 1, 2, \dots, N-1, \quad (18)$$

where \tilde{C}_j is a square matrix of size $[M_j * M_j]$, \tilde{A}_j is a rectangular matrix of size $[M_j * M_{j-1}]$, \tilde{B}_j is a rectangular matrix of size $[M_j * M_{j+1}]$, and \mathbf{Y}_j and \mathbf{F}_j are vectors of the same order M_j . One then finds the solution of Eq. (18) in the form

$$\mathbf{Y}_j = \bar{\alpha}_{j+1} \mathbf{Y}_{j+1} + \bar{\beta}_{j+1}, \quad j = N-1, N-2, \dots, 0, \quad (19)$$

where recursion $\bar{\alpha}_j$ is a rectangular matrix of size $[M_{j-1} * M_j]$ and recursion $\bar{\beta}_j$ is an M_{j-1} -dimensional vector [18].

Matrices \tilde{A}_j , \tilde{B}_j , and \tilde{C}_j in (18) for Eqs. (15)–(17) are the following (for each spatial location j):

$$\tilde{A} = \begin{bmatrix} A_{11} & 0 & 0 \\ 0 & A_{22} & 0 \\ 0 & 0 & 0 \end{bmatrix}, \quad \tilde{C} = \begin{bmatrix} C_{11} & C_{12} & C_{13} \\ C_{21} & C_{22} & C_{23} \\ C_{31} & C_{32} & C_{33} \end{bmatrix}, \quad \tilde{B} = \begin{bmatrix} B_{11} & 0 & 0 \\ 0 & B_{22} & 0 \\ 0 & 0 & 0 \end{bmatrix}.$$

The coefficients for the matrix elements for finite-difference approximation with PML are given in Appendix A.

For the oblique incidence case ($k_{x_0} \neq 0$), one can use a split-step algorithm, first solving the Schrödinger type Eqs. (15)–(17) without lower-order terms (the first derivative of the function). Secondly, the solutions are to be found for the hyperbolic equations

$$\frac{\partial E_x}{\partial t} = k_{x_0} \frac{\partial E_z}{\partial z}, \tag{20}$$

$$\frac{\partial E_z}{\partial t} = k_{x_0} \frac{\partial E_x}{\partial z}. \tag{21}$$

Introducing the variables $E_+ = E_x + E_z$ and $E_- = E_x - E_z$ we obtain the equations for the E_+ and E_- :

$$\frac{\partial E_+}{\partial t} = +k_{x_0} \frac{\partial E_+}{\partial z}, \tag{22}$$

$$\frac{\partial E_-}{\partial t} = -k_{x_0} \frac{\partial E_-}{\partial z}. \tag{23}$$

Eqs. (22) and (23) can be solved with the explicit method using upwind difference discretization, and because of the waves absorbed in the PML layer during calculations in the previous step, we do not have to solve Eqs. (22) and (23) in the PML layer. For an explicit method, we are required to choose the time step satisfying the Courant–Friedrichs–Lewy stability condition

$$\Delta t \leq \frac{\Delta x}{|v|}.$$

Finally, the electric field components E_x and E_z are derived from E_+ and E_- .

As to the boundary conditions for the general case of a magnetized plasma when the external magnetic field is at an angle with the z -axis, they are similar to the ones discussed earlier for the isotropic case. However, certain details should be taken into account. The equation for the left boundary arising from the boundary condition (10) is used to obtain the starting values for recursive relation matrices $\bar{\alpha}_1$ and $\bar{\beta}_1$ at $z = 0$ by comparing it with the

$$\begin{pmatrix} E_x \\ E_y \\ E_z \end{pmatrix}_0 = \begin{vmatrix} \alpha_{11} & 0 & 0 \\ 0 & \alpha_{22} & 0 \\ 0 & 0 & \alpha_{33} \end{vmatrix}_1 \begin{pmatrix} E_x \\ E_y \\ E_z \end{pmatrix}_1 + \begin{pmatrix} \beta_1 \\ \beta_2 \\ \beta_3 \end{pmatrix}_1. \tag{24}$$

Note that the intensity of the incident radiation in the general case of a magnetized medium, when the external magnetic field is at an angle with the z -axis, is determined by all three components of the electric field vector, and so the amplitude of the upward going wave E_+ at the left boundary should be corrected with the factor as follows:

$$E_+ = \frac{E_+}{\sqrt{1 + |K|^2 + |B|^2}}, \tag{25}$$

where the coefficients K and B are sometimes called polarization coefficients [23] and they are found from any of the two Eqs. (15)–(17):

$$K = \frac{E_y}{E_x}, \quad B = \frac{E_z}{E_x}. \tag{26}$$

Also, one should note that the polarization coefficients would affect coefficients β_2 and β_3 in Eq. (24).

Finally, at the right boundary we use the absorbing boundary conditions similar to the ones that were used for the isotropic case.

7. Two-dimensional wave propagation in inhomogeneous magnetoactive plasmas

We have discussed the problem of the wave propagation in an isotropic medium (1D scalar equation) and in the general case of an anisotropic medium (1D vector equations). In this section, we shall investigate the reflection from the ionosphere with a more complicated 2D model of electron density, approximating the density artificially created in ionospheric modification experiments.

For 1D scalar or vector equations, we solved the tridiagonal or block-tridiagonal systems of linear equations arising from the implicit FD approximations. However in the two-dimensions, the penta-diagonal matrix occurs in the implicit FD approximations that cannot be efficiently solved with the above-mentioned approach. Here, we consider the ADI methods to solve 2D Eqs. (15)–(17).

In the most common ADI approach, a variation of the Crank–Nicholson approximation is used, which is efficient especially for rectangular computational domain. Here, we use the scheme based on the Douglas high-order accurate method [28] which in two dimensions coincides with the Peaceman–Rachford method [19]. First, we consider the McKee and Mitchell scheme [21] with mixed-derivative term. McKee and Mitchell [21] approximated the parabolic equation with mixed derivative as straightforward Taylor expansions of operators in a general two-level finite-difference formula.

To derive the scheme for the general case, let us consider the linear equation for the function $U(x, z)$ of the two independent variables x and z . The finite-difference form of equation with mixed-derivative and lower-order terms (first-order derivatives and zero-order term) is the following

$$U_{i,j}^{n+1} - U_{i,j}^n = [r_z c \delta_z^2 + r_x a \delta_x^2 + r'_z e H_z + r'_x l H_x + r_{xz} b H_x H_z + rd] U_{i,j}^n. \quad (27)$$

The derivative approximations are defined as following:

$$\begin{aligned} \delta_x^2 U_{i,j}^n &= U_{i+1,j}^n - 2U_{i,j}^n + U_{i-1,j}^n, \\ \delta_z^2 U_{i,j}^n &= U_{i,j+1}^n - 2U_{i,j}^n + U_{i,j-1}^n, \\ H_x U_{i,j}^n &= U_{i+1,j}^n - U_{i-1,j}^n, \\ H_z U_{i,j}^n &= U_{i,j+1}^n - U_{i,j-1}^n. \end{aligned} \quad (28)$$

$U_{i,j}^n$ is the solution of the difference equation at the grid point (or node) of the discretized domain. The nodal coordinates are $x = i\Delta_x$, $z = j\Delta_z$, $t = n\tau$ with grid spacing Δ_x and Δ_z , and τ is the time step. r_x , r_z , r_{xz} , r'_z , r'_x , r arise after finite-difference approximation and for Eqs. (15)–(17) they are

$$r_x = \frac{\tau}{\Delta_x^2}, \quad r'_x = \frac{\tau}{2\Delta_x}, \quad r_z = \frac{\tau}{\Delta_z^2}, \quad r'_z = \frac{\tau}{2\Delta_z}, \quad r_{xz} = \frac{\tau}{4\Delta_x\Delta_z}, \quad r = \tau,$$

$a = c = i$, $b = -i$, $l = 0$, $e = k_{x_0}$ are constants in the operators (second-order, mixed, and first-order derivatives) in normalized Eqs. (15)–(17),

$$d = i \frac{L}{z_0} \varepsilon_{i'j'} - ik_{x_0}^2, \quad i', j' = \{x, y, z\}.$$

Following the prescription of McKee and Mitchell [21], Eq. (27) can be approximated with a general two-level finite-difference formula. The difference operators at the advanced time level of scheme $U_{i,j}^{n+1}$ can be factorized with the appropriate choice of coefficients at the difference operators so that the scheme becomes

$$\left[(1 + \bar{D}\delta_x^2 + \bar{B}H_x)(1 + \bar{E}\delta_z^2 + \bar{C}H_z) \right] U_{i,j}^{n+1} = \left[(1 + \overset{+}{D}\delta_x^2 + \overset{+}{B}H_x)(1 + \overset{+}{E}\delta_z^2 + \overset{+}{C}H_z) + r_{xz}bH_xH_z + rd \right] U_{i,j}^n. \tag{29}$$

The scheme (29) is capable of factorization by setting \bar{D} , \bar{B} , \bar{E} , \bar{C} , $\overset{+}{D}$, $\overset{+}{B}$, $\overset{+}{E}$, and $\overset{+}{C}$ as following:

$$\begin{aligned} \overset{\pm}{D} &= \frac{1}{f} \pm \frac{1}{2}r_x a, & \overset{\pm}{B} &= \frac{1}{f} \pm \frac{1}{2}r'_x l, \\ \overset{\pm}{E} &= \frac{1}{f} \pm \frac{1}{2}r_z c, & \overset{\pm}{C} &= \frac{1}{f} \pm \frac{1}{2}r'_z e, \end{aligned} \tag{30}$$

where f is an adjustable parameter.

In general, the scheme (29) can be split in the Douglas–Rachford form to yield

$$\begin{aligned} &\left[\left(1 + \left(\frac{1}{f} - \frac{1}{2}r_z c \right) \delta_z^2 + \left(\frac{1}{f} - \frac{1}{2}r'_z e \right) H_z \right) \right] U_{i,j}^{n+1*} \\ &= \left[\left(1 + \left(\frac{1}{f} + \frac{1}{2}r_z c \right) \delta_z^2 + \left(\frac{1}{f} + \frac{1}{2}r'_z e \right) H_z \right) + r_{xz}bH_xH_z + rd + (r_z c \delta_x^2 + r'_z e H_x) \right. \\ &\quad \left. + \frac{1}{f} \left((\delta_z^2 + H_z)(r_x a \delta_x^2 + r'_x l H_x) + (\delta_x^2 + H_x)(r_z c \delta_x^2 + r'_z e H_x) \right) \right] U_{i,j}^n, \end{aligned} \tag{31}$$

$$\left[\left(1 + \left(\frac{1}{f} - \frac{1}{2}r_x a \right) \delta_x^2 + \left(\frac{1}{f} - \frac{1}{2}r'_x l \right) H_x \right) \right] U_{i,j}^{n+1} = U_{i,j}^{n+1*} + \left[\left(\frac{1}{f} - \frac{1}{2}r_x a \right) \delta_x^2 + \left(\frac{1}{f} - \frac{1}{2}r'_x l \right) H_x \right] U_{i,j}^n. \tag{32}$$

In the case, when $e = l = d = 0$, the scheme (31) and (32) coincides with the McKee and Mitchell scheme [21]. Also, this is the Peaceman–Rachford scheme when $f = \infty$ [19], and the high-accuracy Mitchell–Fairweather scheme when $f = 12$ [29]. One can see that Eqs. (31) and (32) involve the solution of two sets of tridiagonal equations at each time step in the z -direction and then x -direction subsequently. One should note that the boundary conditions should be specified at the intermediate level of scheme (31); however, in general, the method can lose accuracy if the boundary conditions are time-dependent. This difficulty may be overcome by reorganizing the computational procedure [22].

We now investigate the stability condition for the general scalar scheme (29). For a two level scalar FD scheme (29), the von Neumann condition is sufficient as well as necessary for stability. The amplification factor (for the scheme without lower-order terms) is complex and the magnitude of the amplification factor is given by

$$\begin{aligned} |\tilde{g}|^2 &= 1 + \tilde{r}_{xz} \sin(\phi) \sin(\psi) \\ &\times \frac{(\tilde{r}_{xz} \sin(\phi) \sin(\psi) - 4r(\sin^2(\phi/2) + \sin^2(\psi/2)) + 32\tilde{f}r \sin^2(\phi/2) \sin^2(\psi/2))}{((1 - 4\tilde{f} \sin^2(\phi/2))^2 + 4r^2 \sin^4(\phi/2))((1 - 4\tilde{f} \sin^2(\psi/2))^2 + 4r^2 \sin^4(\psi/2))}, \end{aligned} \tag{33}$$

where $\phi = m_x \Delta$ and $\psi = m_z \Delta$, m_x and m_z are wave numbers that can be chosen arbitrarily. Here, $\tilde{r}_{xz} = 4r_{xz}$, $r_x = r_z = r$, $\Delta_x = \Delta_z = \Delta$, and $\tilde{f} = 1/f$. It is obvious, that the amplification factor is unity when mixed-derivative term is not taken into account ($\tilde{r}_{xz} = 0$). The presence of this term implies that additional conditions must be imposed $|\phi| \leq \pi$, $|\psi| \leq \pi$ in order for the $|\tilde{g}| < 1$. Provided these conditions are satisfied, one can find the restriction for the value of parameter f .

Now let us turn to the solution of the vector equations. The stability analysis of the scheme (29) for the vector case is more complicated. However, for the scalar case considered above, the stability analysis shows that the presence of mixed-derivative term implies additional conditions for stability. In our case, we shall apply a split-step method to solve first Eqs. (15)–(17) without mixed-derivative term which can be solved on the second step.

Once again, similar to the 1D case of the wave propagation in a magnetized medium, the matrices of coefficients would arise in solving the difference equations. Here we consider the general scheme (29) for the normal incidence case ($k_{x_0} = 0$) without mixed-derivative term and with $f = \infty$. Thus, we have

$$\left[\left(1 - \frac{1}{2} r_x a \delta_x^2 \right) \right] U^{n+1*} = \left[\left(1 + \frac{1}{2} r_x a \delta_x^2 \right) + (r_z c \delta_z^2 + rd) \right] U_{i,j}^n, \quad (34)$$

$$\left[\left(1 - \frac{1}{2} r_z c \delta_z^2 - \frac{1}{2} rd \right) \right] U_{i,j}^{n+1} = U_{i,j}^{n+1*} - \left[\frac{1}{2} r_z c \delta_z^2 + \frac{1}{2} rd \right] U_{i,j}^n. \quad (35)$$

In order to avoid the problem with boundary conditions at the intermediate level, we split scheme (29) first in the x -direction (ξ – horizontal) and then in the z (ζ – vertical) direction. The finite-difference Eqs. (34) and (35) are solved with block-tridiagonal methods. But unlike the 1D case we have two sets of matrix coefficients $\{\tilde{A}_\xi, \tilde{C}_\xi, \tilde{B}_\xi\}$ and $\{\tilde{A}_\zeta, \tilde{C}_\zeta, \tilde{B}_\zeta\}$ with the components $A_{\xi'j'}, C_{\xi'j'}, B_{\xi'j'}$ and $A_{\zeta'j'}, C_{\zeta'j'}, B_{\zeta'j'}$ ($i', j' = \{x, y, z\}$), which arise when the numerical scheme (34) and (35) is applied to Eqs. (15)–(17). Matrix coefficients in the first set, corresponding to the splitting in the ξ horizontal direction, have only diagonal elements, and coefficients in the second set correspond to the splitting in the ζ vertical direction (see Appendix B).

The split forms (34) and (35) coincide with the Douglas [20] forms in the case of the scalar equations. Now one must specify a boundary value at the end of each line (Eqs. (34) and (35)) being solved via tri-diagonal methods. Since the wave is incident at the lower boundary of the rectangular computational domain, only the lower boundary condition has a physical meaning, so that the boundary condition is applied in the form similar to Eq. (10). At the top boundary, an absorbing boundary condition is applied using the PML technique described above for the 1D case. The right and left boundaries are also absorbing boundaries so that the numerical solution decays exponentially toward these boundaries, and no reflection is allowed.

Finally, on the second step of solving of Eqs. (15)–(17), the mixed-derivative terms are solved. Similar to the 1D case with lower-order derivatives terms we consider the two equations for E_+ and E_- denoted by $E_+ = E_x + E_z$ and $E_- = E_x - E_z$:

$$\frac{\partial E_+}{\partial t} = -i \frac{\partial^2 E_+}{\partial x \partial z}, \quad (36)$$

$$\frac{\partial E_-}{\partial t} = +i \frac{\partial^2 E_-}{\partial x \partial z}. \quad (37)$$

We use a predictor–corrector type of the method to solve Eqs. (36) and (37) (see Appendix C). Here the mixed-derivative terms are usually treated explicitly. The amplification factor for this scheme is

$$|\tilde{g}| = \sqrt{\left(1 \mp \frac{1}{2} \rho^2 \sin^2(\phi) \sin^2(\psi) \right)^2 + \rho^2 \sin^2(\phi) \sin^2(\psi)}$$

and it can be presented as

$$|\tilde{g}| = \sqrt{1 + \Delta_t^2 f_1(\phi, \psi) + \Delta_t^4 f_2(\phi, \psi)},$$

where functions $f_1(\phi, \psi)$ and $f_2(\phi, \psi)$ are bounded. If m_1 and m_2 are maximum values of $|f_1(\phi, \psi)|$ and $|f_2(\phi, \psi)|$ with varying ϕ and ψ , then we have

$$|\tilde{g}| \leq \sqrt{1 + m_1 \Delta_t^2 + m_2 \Delta_t^4} = 1 + O(\Delta_t)^2.$$

Thus this stability condition does not impose additional restriction on time step satisfying the stability condition of the scheme for hyperbolic model equations ($k_{x_0} \neq 0$).

8. One-dimensional simulation results

In this section, we shall consider numerical examples for 1D propagation of the full-wave in an inhomogeneous isotropic and magnetized media. The results of calculations demonstrate the standing wave patterns of a HF radio wave totally or partially reflected from the ionosphere and the application of the PML technique for the open-domain problem.

For the case of 1D propagation in an isotropic medium and normal incidence of the wave, the wave equation (13) is solved either for E_x or E_y , and the E_z component is zero. First, we consider wave propagation in a uniform density so that there is no reflection point. In this case, the wave should propagate up to the right boundary and then escape to infinity. Therefore, the PML absorbing boundary condition is required at the right boundary. However, in the absence of PML, there is a strong reflection when the Dirichlet condition is applied at the right boundary as one can see in Fig. 1. In Fig. 2, we represent the results of simulations with PML boundary conditions, which demonstrate that the energy of the incident wave with unit amplitude is absorbed inside the PML region and no reflection occurs from the right boundary. The wave amplitude of unity for the wave outside the PML region is unchanged.

In the PML implementation, one must construct the PML layer with the finite thickness and choose the damping function $\gamma(z)$, which is nonzero only inside the PML region. In the work of Collino [11], the thickness of the PML layer was optimized in order to minimize the reflection coefficient from the boundary. In that study of the paraxial wave equation, the dependence of the reflection coefficients on the number of the points per wavelength was investigated. The number of the points per wavelength was considered from 5 to 40 and it was found that it is the order of magnitude of the absorbing function that is mainly important [11]. The choice of the function $\gamma(z)$ can be arbitrary and for our problems we use a function in a form of a geometrical progression [10]

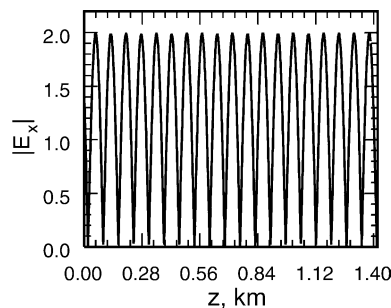


Fig. 1. The electric field amplitude (the reflecting right boundary).

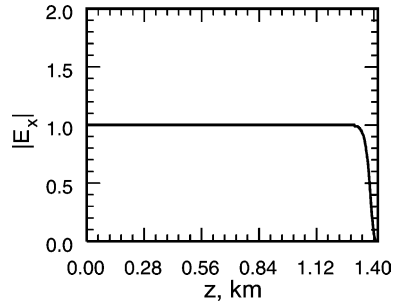


Fig. 2. The electric field amplitude (the PML absorbing right boundary).

$$\gamma(z) = \gamma_0(g^{1/\Delta_z})^z, \quad (38)$$

where Δ_z is the vertical resolution of the grid. The length of the PML layer used in Fig. 2 is about 1.2 wavelengths (32 grid points) with 26 grid points per wavelength, and $\Delta_z = 60/512 = 0.117$. To quantify the results, we calculate the standard deviation from the amplitude of the incident wave (unity). For the maximum value of the damping function $\max(\gamma(z)) = 11.4$, the standard deviation was about 0.13%. For the calculation with the 18 points per wavelength and similar profile of the absorbing function (the 32 points PML layer) with a maximum of 22.8, the deviation was about 0.185%. We also performed the calculations for the case when a 10 point PML layer was constructed from the values of the coefficients given by Collino [11]. These coefficients were optimized in order to minimize the reflection induced by the boundary for 5 points per wavelength Collino [11, Table 3]. With these coefficients, the standard deviations were 0.75% and 0.62% for the calculations with 26 and 18 points per wavelength, respectively. For the case with less than 5 points per wavelength, the deviation was 1.73%, and it dropped to 1.63% when the amplitude of the coefficients was adjusted so that the maximum value of the coefficients was about 5.022. For the same case with 5 points per wavelength calculation, the PML layer with 5 optimized coefficients from Collino [11, Table 3] was used, which resulted in a standard deviation of 2.73%. These simulations show that the length of the PML layer should be at least comparable to one wavelength, and beyond a small number of points per wavelength, the accuracy does not improve. However, better results can be achieved when the length of the PML layer is about two wavelengths.

In Fig. 3(a), the electric field pattern is shown for a narrow density layer (Fig. 3(b)). Even though the peak density is overdense, there is only partial reflection from the density layer because the thickness of the

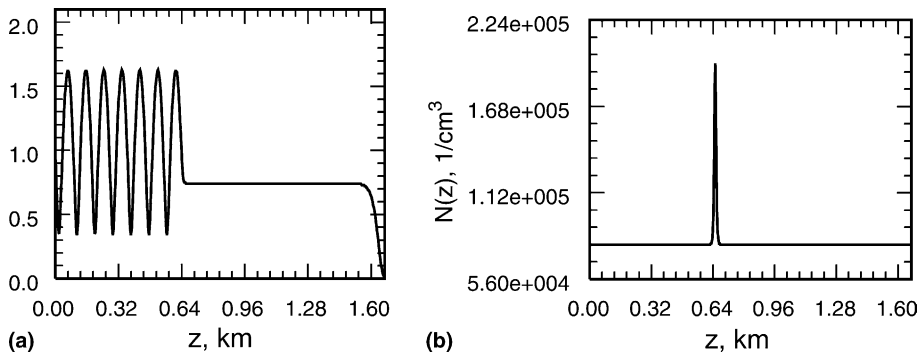


Fig. 3. (a) The amplitude of the electric field as a function of altitude for the case of an unmagnetized plasma with (b) the narrow electron density layer (the peak density is overdense).

density layer is smaller than one wavelength. One can see that after reflection the wave propagates further and is then absorbed in the 32 point PML layer.

We now investigate the solutions of the differential Eqs. (15)–(17) for the linear electron density profile, $N(z) = 1 + (z - z_c)/L$, where L is the density inhomogeneity and z_c is the critical surface where the local plasma frequency matches the given wave frequency. We use the sets of parameters for the F and E regions at Tromsø given by Lundborg and Thide [30]. They used analytical formulae [31] for calculating the wave pattern of a HF radio wave incident vertically into the ionosphere without taking into account the coupling between the ordinary and extraordinary modes that can occur around the reflection regions for the cases when the angle α between magnetic field and vertical is large enough to exclude the conversion of the ordinary mode O to the Z -mode.

In Figs. 4(a)–(c), we show the results of simulations for the parameters of the F region at Tromsø. Here $\omega = 2\pi \cdot 5.423$ MHz, the electron cyclotron frequency $\omega_c = 2\pi \cdot 1.3$ MHz, $L = 50$ km, angle $\alpha = 13^\circ$. In Fig. 4(a), we present the real parts of the refractive index function $n_{O,X}^2$ (the solution of the dispersion Eq. (4)) for the O -mode (filled circle curve) and X -mode (filled-diamond curve). The O -mode refractive index has a zero (vertical solid curve in Fig. 4(a)) at $V = 1$, where $V = \omega_{pe}^2/\omega^2$, ω_{pe} is electron plasma frequency. The reflection points for the X -mode are at $V = 1 \pm Y$, where $Y = \omega_c/\omega$. The refractive index of the X -mode n_X^2 goes to infinity at

$$V = \frac{1 - U}{1 - U \cos^2 \alpha}, \quad U = Y^2. \tag{39}$$

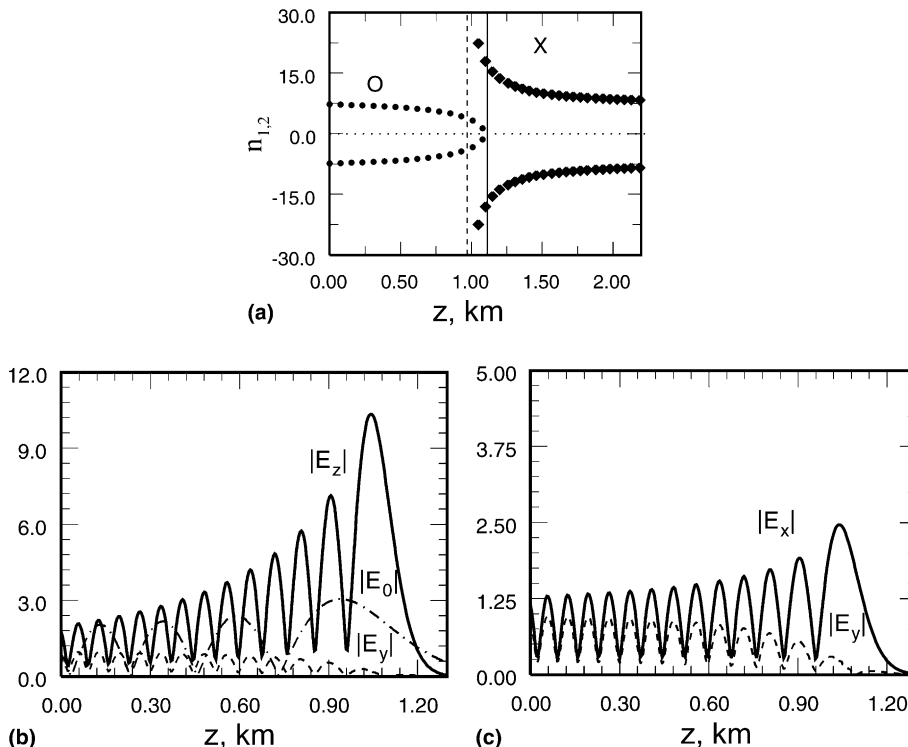


Fig. 4. (a) The refractive index function $n_{O,X}$ (linear density profile, the F region at Tromsø); electric field amplitudes (b) $|E_z|$, $|E_y|$, and for the isotropic case $|E_0|$; (c) $|E_x|$ and $|E_y|$.

The distance between the reflection point of the ordinary wave and the resonance of the X wave is about 151 m and the modes are separated. In Fig. 4(b), we show the $|E_z|$ and $|E_y|$ components of the electric field (solid and dashed lines) and also for the isotropic case, the electric field $|E_0|$ (dash-dotted curve). In Fig. 4(c), we show the $|E_x|$ (solid line) and $|E_y|$ (dashed line) components of the electric field. Note that in this calculation the O -mode was incident normally at the left boundary with unit amplitude and the right boundary was the absorbing boundary approximated with a 10 point PML with the maximum of the damping function $\max(\gamma(z)) = 15.1$. For this case, the choice of the PML layer is not that important since the wave is almost completely reflected at $V = 1$. The spatial grid size Δ_z for the calculations in Figs. 4(b)–(c) was about 0.05.

The results of our calculations for the set of parameters for the E region of Tromsø are shown in Figs. 5(a)–(c). The corresponding parameters for the E layer were $\omega_e = 2\pi \cdot 1.4$ MHz, $L = 5$ km, $\omega = 2\pi \cdot 3.515$ MHz, $\alpha = 13^\circ$. The behavior of the refractive index in Fig. 5(a) is similar to the one in Fig. 4(a) but the resonance layer now is very close to the reflection height of the O -mode (they are separated by about 47 m). There is only partial reflection of the ordinary wave at $V \approx 1$. The wave is partly transmitted as a second branch of the extraordinary wave, which can propagate for $V \geq V_{X_\infty}$ (V_{X_∞} is the resonance layer (39)). Therefore even at normal incidence in the magnetic field, the plasma wave can be excited in the neighborhood of the V_{X_∞} . This is demonstrated in Fig. 5(b), where there is a sharp increase in the amplitude of the $|E_z|$ component (solid line) prior to the reflection layer of the ordinary mode. However, electrostatic waves are not described within a cold plasma model. In this case, the inclusion of electron collisions is the only

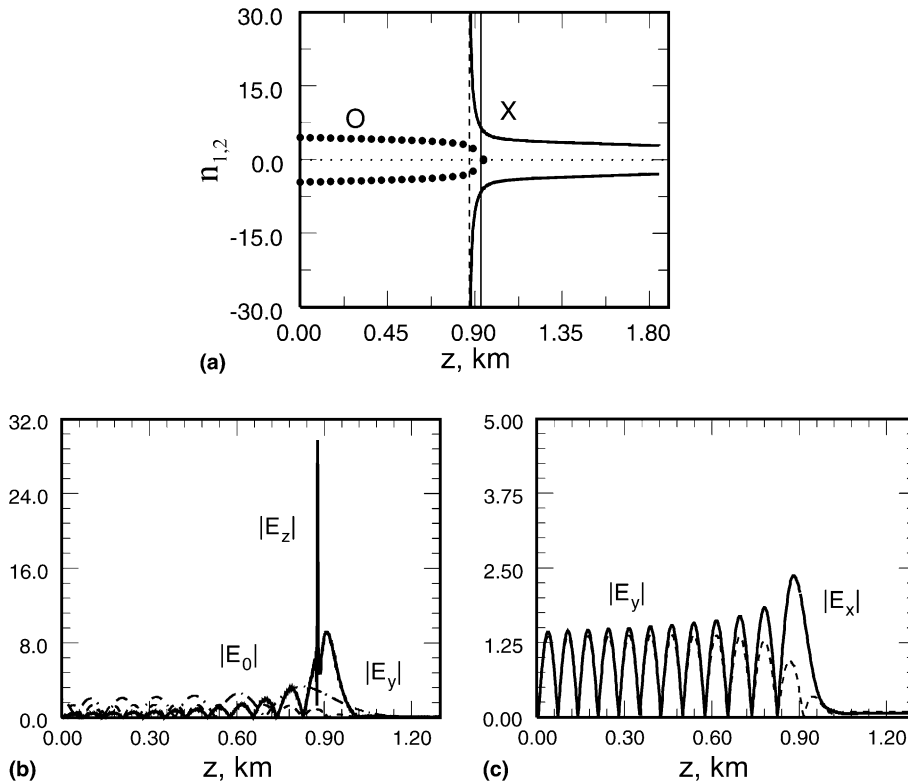


Fig. 5. (a) The refractive index function $n_{o,x}$ (linear density profile, the E region at Tromsø); electric field amplitudes (b) $|E_z|$, $|E_y|$, and for the isotropic case $|E_0|$; (c) $|E_x|$ and $|E_y|$.

mechanism to resolve the singularity that occurs when the wave approaches the plasma resonance. Here, we used $\nu = 10^3 \text{ s}^{-1}$. The resolution in space for these calculations was about 87 cm per grid size. The normalization of the incident wave was the same as in the previous case and the right absorbing boundary was approximated with about 1.5 wavelength PML in the form of (38) and $\max(\gamma(z)) = 30.77$.

Here, we investigate the wave propagation for a model of a sporadic E layer at Tromsø, which is approximated with the parabolic model for the electron density, $N(z) = \omega_{\text{cr}}^2/\omega^2[1 - (z - z_c)^2/L^2]$, where L is the half-thickness of the layer, z_c is the height of the density peak, the critical frequency ω_{cr} is the maximum plasma frequency of the profile, and $\omega_{\text{cr}} = \omega$ [30]. The peak density is about $N_{\text{max}} = 1.53 \times 10^5 \text{ cm}^{-3}$. The corresponding parameters are $\omega_e = 2\pi \cdot 1.3 \text{ MHz}$, $L = 1 \text{ km}$, $\omega = 2\pi \cdot 3.515 \text{ MHz}$, $\nu = 10^4 \text{ s}^{-1}$, and $\alpha = 13^\circ$. The real part of refractive index function $n_{O,X}^2$ is shown in Fig. 6(a). There are two reflection points for the O -mode (solid vertical lines in Fig. 6(a)), and they are very close to the poles of the X -mode (dashed vertical lines). In Fig. 6(b) we show the $|E_z|$ and $|E_y|$ components of the electric field (solid and dashed lines) and also for the isotropic case, the electric field $|E_0|$ (dash-dotted curve). In Fig. 6(c), the $|E_x|$ (solid line) and $|E_y|$ (dashed line) electric field components are shown.

In this case, the O -mode is partially reflected and directly converted into the electrostatic mode. The O -mode penetrates further than the layer $V = 1$ and continues in the Z -mode. However, the peak density is too low for the Z -mode to be reflected at the layer $V = 1 + Y$ (the Z -mode critical density is about $2.1 \times 10^5 \text{ cm}^{-3}$). Thus the Z wave penetrates through the layer that results in the reflection above the density peak height at $z \simeq 0.76 \text{ km}$, and the resonance at $z \simeq 0.78 \text{ km}$ (the second spike in Fig. 6(b)).

Also, one can see that the amplitude of the electric field $|E_z|$ is very high when compared to the electric field for the isotropic case (Fig. 6(b)). The grid size for this calculation was $\Delta_z = 0.047$ and the length of the PML boundary layer was about one wavelength (80 m or 30 points) with $\max(\gamma(z)) = 28.8$.

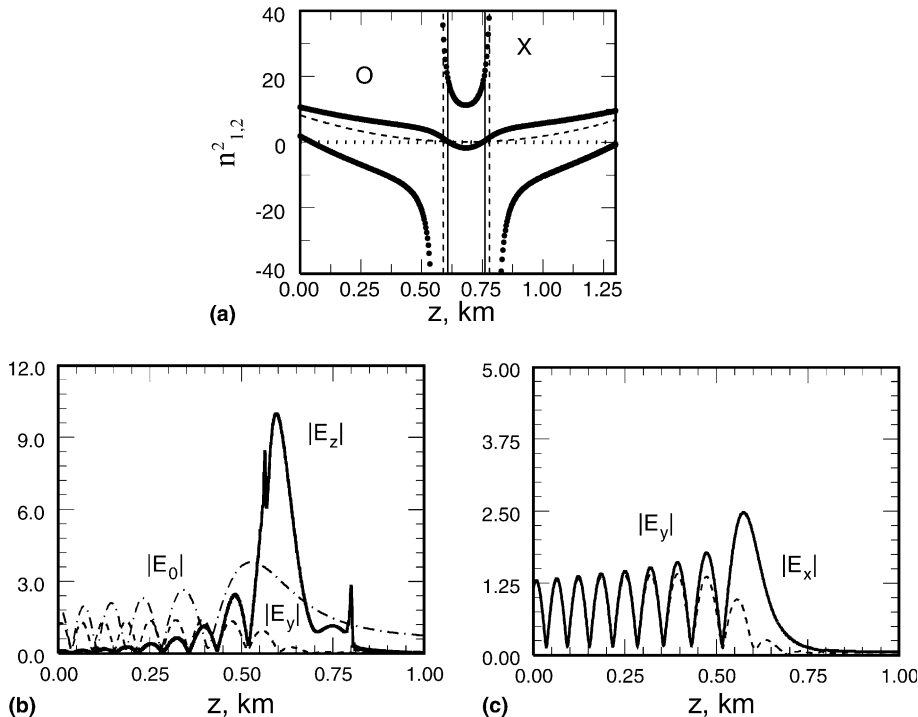


Fig. 6. (a) The refractive index function $n_{O,X}^2$ (parabolic density profile, the E region at Tromsø); electric field amplitudes (b) $|E_z|$, $|E_y|$, and for the isotropic case $|E_0|$; (c) $|E_x|$, $|E_y|$.

9. Two-dimensional simulation results

For the 2D simulations of the wave propagation in a density with the overdense blobs in the E layer at Arecibo, we use a model of a 2D electron density profile to approximate the electron density patch associated with the sporadic- E layer [4]. Here, we consider the 2D density profile (shown in Fig. 7) $N(x, z) = N_0[1 + \tilde{N}_{\max} \exp(-(x - x_c)^2/L_x^2 - (z - z_c)^2/L_z^2)]$ with the characteristic height in the z -direction $L_z = 0.25$ km and characteristic width in the x -direction $L_x = 2$ km. z_c and x_c are the height and the width of the patch center. $N_0 = 0.2 \times 10^5 \text{ cm}^{-3}$ and the peak density is $2.2 \times 10^5 \text{ cm}^{-3}$.

The parameter values used in these calculations are typical for the E region at Arecibo [4]. They are the wave frequency $\omega = 2\pi \cdot 3.175$ MHz, $\alpha = 42^\circ$, the effective electron collision frequency $\nu = 7.387 \times 10^3 \text{ s}^{-1}$, and the electron cyclotron frequency $\omega_e = 2\pi \cdot 1.1$ MHz. In the experiment, an ordinary mode electromagnetic wave is generated and beamed upward. Usually, the beam passes through the E region because the densities are too low and local plasma frequency cannot match the incident wave frequency. However,

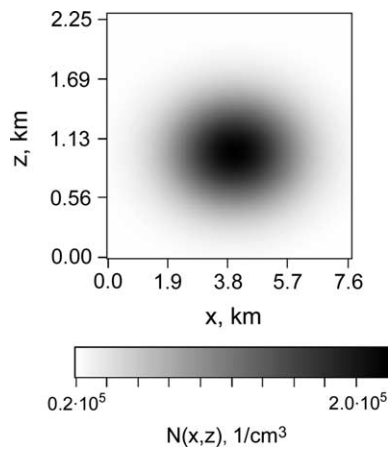


Fig. 7. The 2D electron density profile for the sporadic E region patch at Arecibo.

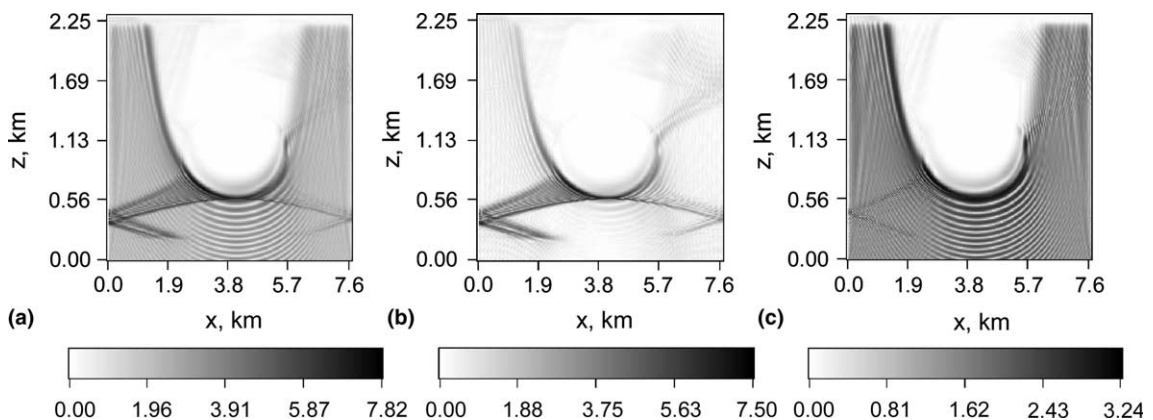


Fig. 8. The contours of field amplitudes (a) the total electric field $|E|$, the components of the electric field (b) $|E_z|$, and (c) $|E_x|$ with the right and the left side Dirichlet boundary conditions. The angle $\alpha = 42^\circ$.

because the overdense patch represented by 2D density profile is in the path of the HF beam, the wave is reflected.

The calculation domain of 516 points in the x and the z -directions was considered. The grid steps $\Delta_x = 15$ m and $\Delta_z = 4.5$ m so that there are about 6 and 21 points per wavelength in the x and z -directions, respectively. For the calculations in Figs. 9 and 10, the resolution in z -direction was increased, so that $\Delta_z = 2.25$ m. In Figs. 8(a)–(c), we display the contours of the total electric field amplitude $|E|$ with $|E_z|$ and $|E_x|$ components. Here, the Dirichlet boundary conditions were applied at the right and the left sides of the computational domain. The wave with the amplitude normalized to unity was incident at the lower boundary of the domain, and the top boundary was approximated with about a 1.5 wavelengths PML layer. Although the wave was incident vertically, one would expect some reflection from the right and the left boundaries because of the 2D electron density profile. Indeed, one can see strong reflection from the left side (the asymmetry arises due to finite angle α) in Figs. 8(a) and (b). This reflection affects propagation in

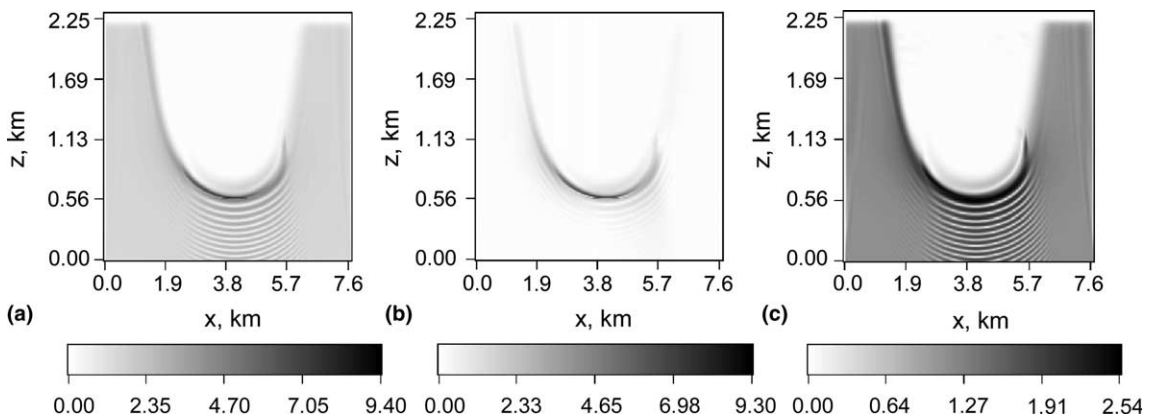


Fig. 9. The contours of electric field amplitudes (a) $|E|$, (b) $|E_z|$, and (c) $|E_x|$ with the right and the left side PML boundary conditions. The angle $\alpha = 42^\circ$.

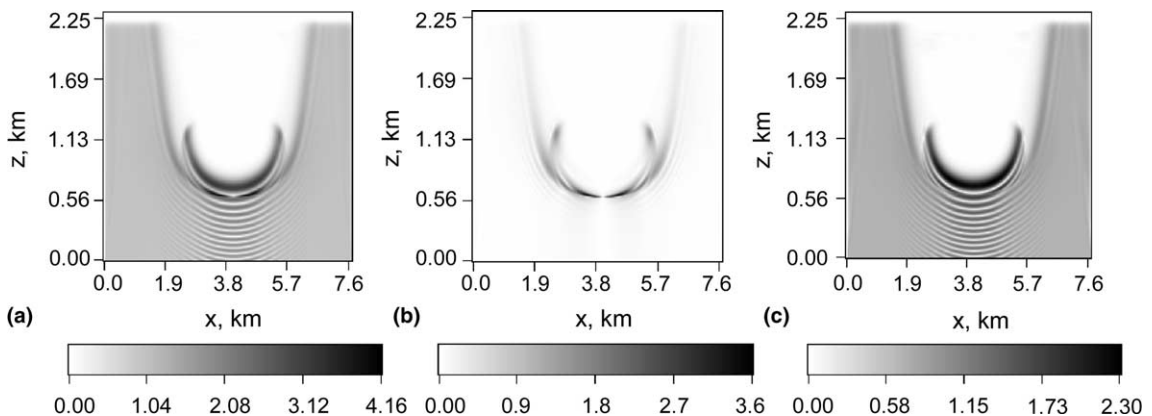


Fig. 10. The contours of electric field amplitudes (a) $|E|$, (b) $|E_z|$, and (c) $|E_x|$ with the right and the left side PML boundary conditions. The angle $\alpha = 0^\circ$.

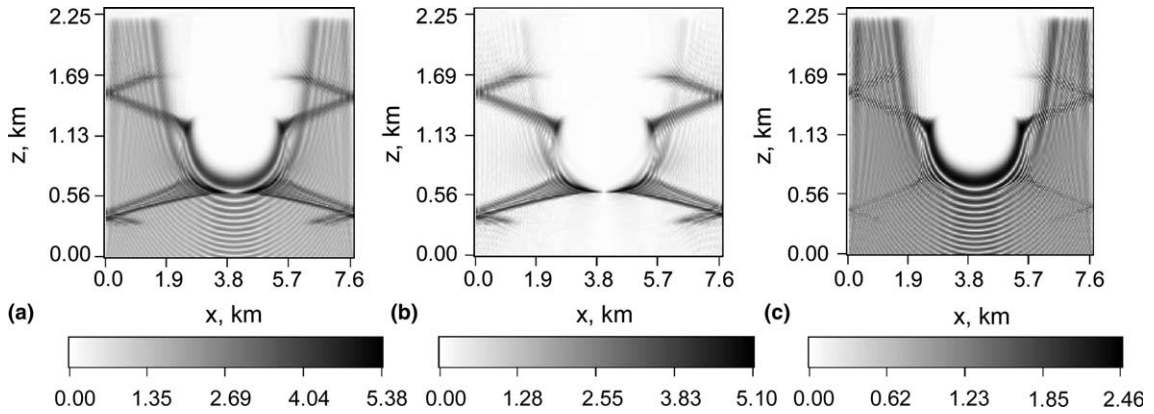


Fig. 11. The contours of electric field amplitudes (a) $|E|$, (b) $|E_z|$, and (c) $|E_x|$ with the right and the left side Dirichlet boundary conditions. The angle $\alpha = 0^\circ$.

the z -direction so that the PML boundary at the top cannot absorb the wave (seen more clearly in Fig. 8(c)). Here, there was no steady-state solution and the run was eventually ruined.

In order to avoid reflections from the boundaries one should construct the absorbing layers at the right and the left sides of the domain. In Figs. 9(a)–(c), we demonstrate the 2D standing wave patterns for the amplitudes of $|E|$, $|E_z|$, and $|E_x|$. There are no visible reflections from the top boundary and from the right and the left side boundaries as well. The length of the horizontal PML layers was about 10 points that is less than two wavelengths. One can see that in the regions of about one kilometer from both sides, the waves propagate vertically, and the amplitude of the total electric field (Fig. 9(a)) is unity.

In Figs. 10(a)–(c), similar calculation experiments were performed for the case when the angle $\alpha = 0$ for the 2D density profile shown in Fig. 7. The same PML layers were used at the boundaries. As the result, we can see symmetric standing wave patterns with the maximal amplitudes at $z = 0.74$ km that is the region of first reflection of the O -mode and near $x = b_x/2$, where b_x is the size of the computational box profile in the x -direction (Figs. 10(a)–(b)). Note that for normal incidence when $\alpha = 0$, the amplitude of the $|E_z| \neq 0$ because of density inhomogeneity, although it is smaller than that for the case when $\alpha \neq 0$. However, at $x = b_x/2 \sim 4$ km, the amplitude of the $|E_z|$ is almost zero and only the $|E_x| \neq 0$ (because the O -mode and the X -mode are uncoupled). In order to demonstrate the effect of PML boundaries in the x -direction, similar to the case of finite angle α , we turn off the PML boundaries by simply setting function $\gamma(x) = 0$ in the PML layer of the computation domain. The results of calculations are shown in Figs. 11(a)–(c). One can see the waves are reflected from the right and the left boundaries symmetrically. However, after a while the reflections from the boundaries affect the propagation in all directions resulting in the increase of the amplitude of the wave at the boundaries, and eventually completely ruining the pattern of the fields.

10. Conclusions

We have presented the 1D and 2D numerical models for the propagation of HF radio waves in inhomogeneous magnetized plasmas. The models are utilized for simulating the propagation of the waves that are totally or partially reflected from the ionosphere. The simulations allow one to describe the process of linear conversion of electromagnetic waves into electrostatic waves when the ordinary waves are normally (or obliquely) incident from the lower boundary (in 2D case). The models take into account the geomagnetic field and collisions. The standing wave patterns for the components of the full 3D wave at the reflection and resonant regions are calculated.

The numerical schemes for solving 2D wave propagation time-dependent equations and 1D vector and scalar equations as their limits, are derived. The model employed the Maxwellian PML technique for approximating nonreflecting arbitrary boundary conditions. The Maxwellian PML technique is very convenient for realization and can be applied to various numerical models. We have demonstrated the effectiveness of the PML technique for transparent boundary conditions for an open-domain problem with 1D and 2D numerical examples.

Appendix A. Matrix coefficients for block-tridiagonal solver with PML for 1D vector equation

The coefficients for matrices $\tilde{A}_j, \tilde{C}_j, \tilde{B}_j$ in (18) for Eqs. (15)–(17) (for each spatial location j) are the following:

$$\begin{aligned}
 A_{11} &= A_{22} = -\left(i \frac{\tau}{2A_z^2}\right) \left(\frac{1}{2} \bar{g}_z\right), \\
 A_{33} &= 0, \quad A_{i'j'} = 0 \quad (i' \neq j'), \quad i', j' = \{1, 2, 3\}, \\
 B_{11} &= B_{22} = -\left(i \frac{\tau}{2A_z^2}\right) \left(\frac{1}{2} g_z^+\right), \\
 B_{33} &= 0, \quad B_{i'j'} = 0 \quad (i' \neq j'), \quad i', j' = \{1, 2, 3\}, \\
 C_{11} &= \frac{1}{g_z} + \left(i \frac{\tau}{2A_z^2}\right) \left(\frac{1}{2} g_z^\pm\right) - \left(i \frac{\tau L}{2z_0}\right) \frac{1}{g_z} \varepsilon_{xx}, \\
 C_{22} &= \frac{1}{g_z} + \left(i \frac{\tau}{2A_z^2}\right) \left(\frac{1}{2} g_z^\pm\right) - \left(i \frac{\tau L}{2z_0}\right) \frac{1}{g_z} \varepsilon_{yy} + \left(i \frac{\tau k_x^2}{2}\right) \frac{1}{g_z}, \\
 C_{33} &= \frac{1}{g_z} - \left(i \frac{\tau L}{2z_0}\right) \frac{1}{g_z} \varepsilon_{zz} + \left(i \frac{\tau k_x^2}{2}\right) \frac{1}{g_z}, \\
 C_{i'j'} &= -\left(i \frac{\tau L}{2z_0}\right) \frac{1}{g_z} \varepsilon_{i'j'} \quad (i' \neq j'), \quad i', j' = \{1, 2, 3\},
 \end{aligned} \tag{A.1}$$

where τ is the time step, A_z is the grid spacing in the z -direction, the Airy length $z_0 = (c^2 L / \omega^2)^{1/3}$ is the normalization parameter for the independent variable z , and L is the scalelength of the density inhomogeneity.

$$\begin{aligned}
 \bar{g}_{z_j} &= (g_{z_{j-1}} + g_{z_j}), \quad g_{z_j}^+ = (g_{z_{j+1}} + g_{z_j}), \\
 g_{z_j}^\pm &= (g_{z_{j-1}} + 2g_{z_j} + g_{z_{j+1}}), \\
 g_z &= \frac{1}{s_z} = \frac{1}{1 + i\gamma_z(z)}
 \end{aligned} \tag{A.2}$$

is the absorbing function which depends on z .

Appendix B. Matrix coefficients for block-tridiagonal solver with PML for 2D vector equation

Matrix coefficients for each spatial location i in the horizontal direction ξ :

$$\begin{aligned}
A_{\xi_{yy}} &= A_{\xi_{zz}} = -\left(\frac{r_x a}{2}\right) \left(\frac{1_-}{2} g_{\xi_i}^-\right), \\
A_{\xi_{xx}} &= 0, \quad A_{\xi_{i'j'}} = 0 \quad (i' \neq j'), \\
B_{\xi_{yy}} &= B_{\xi_{zz}} = -\left(\frac{r_x a}{2}\right) \left(\frac{1_+}{2} g_{\xi_i}^+\right), \\
B_{\xi_{xx}} &= 0, \quad B_{\xi_{i'j'}} = 0 \quad (i' \neq j'), \\
C_{\xi_{xx}} &= 1, \quad C_{\xi_{yy}} = C_{\xi_{zz}} = 1 + \left(\frac{r_x a}{2}\right) \left(\frac{1_{\pm}}{2} g_{\xi_i}^{\pm}\right), \\
C_{\xi_{i'j'}} &= 0 \quad (i' \neq j'), \quad i', j' = \{x, y, z\},
\end{aligned} \tag{B.1}$$

where

$$\begin{aligned}
\bar{g}_{\xi_i}^- &= g_{\xi_i}^-(g_{\xi_{i-1}}^- + g_{\xi_i}^-), \quad \bar{g}_{\xi_i}^+ = g_{\xi_i}^+(g_{\xi_{i+1}}^+ + g_{\xi_i}^+), \\
\bar{g}_{\xi_i}^{\pm} &= g_{\xi_i}^{\pm}(g_{\xi_{i-1}}^{\pm} + 2g_{\xi_i}^{\pm} + g_{\xi_{i+1}}^{\pm}),
\end{aligned} \tag{B.2}$$

and

$$g_{\xi_i}^{\pm} = \frac{1}{s_x} = \frac{1}{1 + i\gamma_x(x)}$$

is the absorbing function which depends on x .

Matrices of the coefficients in the second set correspond to the splitting in the vertical direction ζ (for each spatial location j):

$$\begin{aligned}
A_{\zeta_{xx}} &= A_{\zeta_{yy}} = -\left(\frac{r_z c}{2}\right) \left(\frac{1}{2} \bar{g}_{\zeta_j}^-\right), \\
A_{\zeta_{zz}} &= 0, \quad A_{\zeta_{i'j'}} = 0 \quad (i' \neq j'), \\
B_{\zeta_{xx}} &= B_{\zeta_{yy}} = -\left(\frac{r_z c}{2}\right) \left(\frac{1}{2} g_{\zeta_j}^+\right), \\
B_{\zeta_{zz}} &= 0, \quad B_{\zeta_{i'j'}} = 0 \quad (i' \neq j'), \\
C_{\zeta_{xx}} &= C_{\zeta_{yy}} = 1 + \left(\frac{r_z c}{2}\right) \left(\frac{1}{2} g_{\zeta_j}^{\pm}\right) - \frac{rd_{i'j'}}{2} \quad (i' = j'), \\
C_{\zeta_{zz}} &= 1 - \frac{rd_{zz}}{2}, \quad C_{\zeta_{i'j'}} = -\frac{rd_{i'j'}}{2} \quad (i' \neq j'), \quad i', j' = \{x, y, z\},
\end{aligned} \tag{B.3}$$

where $\bar{g}_{\zeta_j}^+$, $g_{\zeta_j}^+$, $\bar{g}_{\zeta_j}^{\pm}$ are determined similar to (B.2) and

$$g_{\zeta_j}^{\pm} = \frac{1}{s_z} = \frac{1}{1 + i\gamma_z(z)}$$

is the absorbing function which depends on z .

Appendix C. Two-step method for solving equations with mixed-derivative terms

Eqs. (36) and (37) are solved with a two-step method when the value of the function at $n + 1$ step depends on the values at the previous n step and intermediate one. In the first step we calculate the

intermediate values for E_+^* and E_-^* using explicit finite difference approximations. This is so called the predictor step. In the next step, the corrector step, using predicted values E_+^* and E_-^* and “old” values E_+^n and E_-^n , the final values for the functions at $n + 1$ step are obtained:

$$E_{\pm}^* = E_{\pm}^n \mp i \frac{\tau}{4\Delta_x \Delta_z} [H_{xy}] E_{\pm}^n, \quad (\text{C.1})$$

$$E_{\pm}^{n+1} = E_{\pm}^n \mp i \frac{\tau}{4\Delta_x \Delta_z} [H_{xy}] \frac{1}{2} (E_{\pm}^n + E_{\pm}^*), \quad (\text{C.2})$$

where the finite difference approximation of mixed derivative

$$H_{xy} E_{i,j}^n = E_{i+1,j+1}^n - E_{i-1,j+1}^n - E_{i+1,j-1}^n + E_{i-1,j-1}^n.$$

References

- [1] P.A. Bernhardt, New system for space based monitoring of ionospheric irregularities and radio wave scintillations, in Space Weather, Geophys. Monogr. 125 (2001) 431.
- [2] F.T. Djuth, P.A. Bernhardt, C.A. Tepley, J.A. Gardner, M.C. Kelley, A.L. Broadfoot, L.M. Kagen, M.P. Sulzer, J.H. Elder, B. Isham, C. Brown, H.C. Carlson, Production of large airglow enhancement via wave-plasma interaction in Sporadic-E, Geophys. Res. Lett. 26 (1999) 1557.
- [3] L.M. Kagan, M.C. Kelley, F. Garcia, P.A. Bernhardt, F.T. Djuth, M.P. Sulzer, C.A. Tepley, The structure of electromagnetic wave-induced 557.7-nm emission associated with a sporadic-E event over Arecibo, Phys. Rev. Lett. 85 (2000) 218–221.
- [4] P.A. Bernhardt, The modulation of sporadic-E layers by Kelvin–Helmholtz billows in the neutral atmosphere, Atmos. Sol.-Terr. Phys. 64 (2002) 1487–1504.
- [5] P.A. Bernhardt, L.M. Duncan, The feedback-diffraction theory of ionospheric heating, J. Atmos. Terr. Phys. 44 (1982) 1061.
- [6] P.N. Guzdar, P.K. Chaturvedi, K. Papadopoulos, S.L. Ossakow, The thermal self-focusing instability near the critical surface in the high-latitude ionosphere, J. Geophys. Res. 103 (1998) 2231.
- [7] N.A. Gondarenko, P.N. Guzdar, G.M. Milikh, A.S. Sharma, K. Papadopoulos, S.L. Ossakow, Spatio-temporal development of filaments due to the thermal self-focusing instability near the critical surface in ionospheric plasmas, Izv. VUZ Radiophys. 7 (1999) 589.
- [8] M. Israeli, S. Orszag, Approximation of radiation boundary conditions, J. Comput. Phys. 41 (1981) 115.
- [9] J. Larsen, H. Dancy, Open boundaries in short-wave simulations: a new approach, Coastal Eng. 7 (1983) 285.
- [10] J.P. Berenger, A perfectly matched layer for the absorption of electromagnetic waves, J. Comput. Phys. 114 (1994) 185.
- [11] F. Collino, Perfectly matched absorbing layers for paraxial equations, J. Comput. Phys. 131 (1997) 164.
- [12] W.C. Chew, W.H. Weedon, A 3-D perfectly matched medium from modified Maxwell’s equation with stretched coordinates, Microwave Opt. Tech. Lett. 7 (1994) 599.
- [13] Z.S. Sacks, D.M. Kingsland, R. Lee, J.F. Lee, A perfectly matched anisotropic absorber for use as an absorbing boundary condition, IEEE Trans. Antennas Propagation 43 (1995) 1460.
- [14] S.D. Gedney, An anisotropic PML absorbing media for the FDTD simulation of fields in lossy and dispersive media, Electromagnetics 16 (1996) 399.
- [15] S.K. Godunov, V.S. Ryabenkii, Theory of Difference Schemes, An Introduction (Transl. Fizmatgiz, Moscow, 1962), Interscience, 1964; Difference Schemes, Elsevier Science, New York, 1987.
- [16] E. Isaacson, H.B. Keller, Analysis of Numerical Methods, Wiley, New York, 1966.
- [17] R.D. Richtmyer, K.W. Morton, Difference Methods for Initial-Value Problems, Interscience, New York/London, 1967.
- [18] A.A. Samarskii, Theory of Difference Schemes, Interscience, transl. Nauka, Moscow, 1977.
- [19] D.W. Peaceman, H.H. Rachford, The numerical solution of parabolic and elliptic differential equations, SIAM J. 3 (1955) 28.
- [20] J. Douglas Jr., H.H. Rachford, On the numerical solution of heat conduction problems in two or three space variables, Trans. Am. Math. Soc. 82 (1956) 421.
- [21] S. McKee, A.R. Mitchell, Alternating direction methods for parabolic equations in two space dimensions with mixed derivative, Comput. J. 13 (1970) 81.
- [22] G. Fairweather, A.R. Mitchell, A new computational procedure for A.D.I. methods, SIAM J. Numer. Anal. 4 (1967) 163.
- [23] V.L. Ginzburg, The Propagation of Electromagnetic Waves in Plasmas, Pergamon, New York, 1970.

- [24] E. Mjølhus, T. Flå, Direct access to plasma resonance in ionospheric radio experiments, *J. Geophys. Res.* 89 (1984) 3921.
- [25] E. Mjølhus, On linear conversion in a magnetized plasma, *Radio Sci.* 25 (1990) 1321.
- [26] F.L. Teixeira, W.C. Chew, General closed-form PML constitutive tensors to match arbitrary bianisotropic and dispersive linear media, *IEEE Microwave Guided Wave Lett.* 8 (1998) 223.
- [27] F.L. Teixeira, W.C. Chew, Advances in the theory of perfectly matched layers, in: W.C. Chew, J.M. Jin, E. Michielssen, J. Song (Eds.), *Fast and Efficient Algorithms in Computational Electromagnetics*, Artech House, Boston/London, 2001, p. 283.
- [28] J. Douglas Jr., Alternating direction methods for three space variables, *Numer. Math.* 4 (1962) 41.
- [29] A.R. Mitchell, G. Fairweather, Improved forms of the alternating direction methods of Douglas, Peaceman and Rachford, for solving parabolic and elliptic equations, *Numer. Math.* 10 (1964) 610.
- [30] B. Lundborg, B. Thide, Standing wave pattern of HF radio wave in the ionospheric reflection region 2, *Appl. Radio Sci.* 21 (1986) 486.
- [31] B. Lundborg, B. Thide, Standing wave pattern of HF radio wave in the ionospheric reflection region 2, *Appl. Radio Sci.* 20 (1985) 947.